

Evidence for Melt Leakage from the Hawaiian Plume above the Mantle Transition Zone

Saswata Hier-Majumder^{a,b}, Maxim D. Ballmer^{c,d}, Matthew Agius^e,
Catherine Rychert^e, Nicholas Harmon^e

^a*Department of Earth Sciences, Royal Holloway University of London, Egham, Surrey,
TW20 0EX, UK.*

^b*AAAS Science and Technology Policy Fellow, Advanced Scientific Computing and
Research, Office of Science, Department of Energy, Germantown, MD, USA.*

^c*ETH Zürich, Switzerland*

^d*University College London, UK*

^e*University of Southampton, UK*

Abstract

We invert P-to-S receiver function phases converted at the top and the bottom of a low velocity layer (LVL) above the mantle transition zone beneath Hawaii. To separate the thermal and melting related seismic anomalies, we carry out over 10 million rock physics inversions to account for variations arising from the Clapeyron slope of phase transition, bulk solid composition, dihedral angle, and mantle potential temperature. We use two independent seismic constraints to evaluate the temperature and shear wave speed within the LVL. The thermal anomalies reveal the presence of a hot and seismically slow plume stem surrounded by a “halo” of cold and fast mantle material. Contrary to the expected melt distribution, the plume stem contains less than 0.5 vol% melt, while the surrounding LVL contains up to 1.7 vol% melt, indicating lateral transport of the melt. The temperature within the LVL,

Email address: Saswata.Hier-Majumder@rhul.ac.uk (Saswata Hier-Majumder)

calculated from seismic observation of the MTZ thickness, suggests that the observed small degree of melting is aided by the presence of volatiles such as CO₂ and H₂O. We estimate the Hawaiian plume loses up to 1.9 Mt/yr H₂O and 10.7 Mt/yr CO₂ to the LVL, providing a crucial missing flux for global volatile cycle models.

Keywords: Mantle Plume, Transition Zone, LVL, Volatiles, Melting

1. Introduction

Mantle plumes are major pathways for heat (Ballmer et al., 2013) and volatile (Burton et al., 2013; Dasgupta and Hirschmann, 2010; Kelemen and Manning, 2015; Plank and Manning, 2019) transfer from the lower mantle to the surface of the Earth. The interaction between ascending plumes and the surrounding mantle can have significant implications for global volatile cycles. Drastic reduction in the water storage capacity between minerals within and above the mantle transition zone (MTZ) (Kohlstedt et al., 1996) can lead to dehydration melting within the ascending plume (Bercovici and Karato, 2003; Ohtani et al., 2004). Sharp reduction in the melting temperature of carbonated basalts just above the MTZ (Thomson et al., 2016) can also trigger decarbonation melting of recycled oceanic crust components in the plume material atop the MTZ. A partially molten region above the ^{c1} MTZ may provide a reservoir for incompatible elements and volatiles, as they preferentially partition into melts (Aubaud, 2004; Hirschmann and Dasgupta, 2009). The seismically anomalous low velocity layer (LVL)—characterized by 2–3% reduction in shear wave speed (Agius et al., 2017; Hier-Majumder and Courtier,

^{c1} *Authors: the*

18 2011; Hier-Majumder et al., 2014; Tauzin et al., 2010; Vinnik and Farra, 2007)
19 and small amounts (~ 1 vol%) of partial melt (Hier-Majumder and Courtier,
20 2011; Hier-Majumder et al., 2014)—is one such possible reservoir. Among
21 the several tectonic settings in which LVLs are observed (Tauzin et al., 2010;
22 Vinnik and Farra, 2007), their potential role in storing mantle volatiles near
23 subduction zones has been discussed (Hier-majumder and Tauzin, 2017; Sun
24 et al., 2020), but volatile fluxes to the LVLs associated with plumes remains
25 relatively poorly quantified (Dasgupta and Hirschmann, 2010).

26 Sequestration of partial melt from the plume into the LVL can impede
27 the volatile transport to the Hawaiian volcanoes from the lower mantle. The
28 high volatile content of the Hawaiian plume, evidenced by 2.4 Mt/yr CO_2
29 emissions from Kilauea volcano (Burton et al., 2013), is derived from re-
30 cycled oceanic crust (Sobolev et al., 2007), which contains up to 450 ppm
31 H_2O (Bizimis and Peslier, 2015) and 250 ppm CO_2 (Anderson and Poland,
32 2017). Volatile-rich melt generation in the LVL and subsequent interaction
33 between these melts and the plume is indicated by geochemical signatures
34 with mixing trends between multiple reservoirs (Hauri, 2002). Despite this
35 geochemical evidence, geophysical observations of melt loss from the plume
36 and quantification of associated volatile fluxes remained elusive.

37 While heat and mass transfer by mantle plumes to the upper mantle is
38 thought to be interrupted by volatile-rich melt pooling above the mantle tran-
39 sition zone (MTZ) (Bercovici and Karato, 2003), quantifying the magnitudes
40 of melt and dissolved volatile fluxes from seismic anomalies remain challeng-
41 ing, as both elevated temperature and melt have similar seismic signatures
42 (Tauzin et al., 2010; Vinnik and Farra, 2007; Wei and Shearer, 2017; Wolfe

43 et al., 2009, 2011). Previous seismic and rock physics studies of plume-related
44 LVLs either focused on mapping anomalous seismic wave speeds in the LVL
45 (Laske et al., 2009; Tauzin et al., 2010; Vinnik and Farra, 2007) or calculating
46 an average melt fraction (Hier-Majumder et al., 2014). Distinction between
47 the spatial variations due to temperature and melt content has remained dif-
48 ficult, as both sustain low seismic wave speeds. In this work, we overcome
49 this limitation by carrying out a detailed analysis of teleseismic P-to-S phase
50 conversions obtained from permanent and temporary land and ocean bottom
51 broadband seismometers from the “Plume-lithosphere undersea melt exper-
52 iment” (PLUME) (Agius et al., 2017; Laske et al., 2009), quantifying the
53 distribution of both temperature and melt in the LVL beneath Hawaii. Both
54 the high lateral resolution of the previous receiver function work (Agius et al.,
55 2017) combined with our formal accounting of error in the inversions allow
56 us to map the distribution of both temperature and melt in the LVL beneath
57 Hawaii with unprecedented resolution. While a previous study ^{c1}by Hier-
58 Majumder et al. (2014) estimated ~ 1 vol% melting in the Hawaiian LVL,
59 the limited lateral resolution of seismic data in this work was insufficient to
60 map the lateral distribution of melt.

61 ^{c1}In the following section, we present a detailed discussion of the methods
62 of seismic and rock physics analysis, a description of the parameter space,
63 and the method of uncertainty calculation arising from uncertainties in the
64 rock physics inversion. Section 3 outlines the results of the rock physics inver-
65 sion, including a detailed description of the effect of each parameter on the

^{c1} Authors: Text added.

^{c1} Authors: Text added.

66 calculated melt volume fraction. Based on our results, we present a hypoth-
67 esis on plume leakage and its impact on the global volatile cycles in Section
68 4. Finally, we outline the key findings of this work in Section 5. We also
69 derive a zeroth-order equation for volatile flux associated with melt leakage
70 in Appendix A.

71 **2. Methods**

72 *2.1. Receiver functions*

73 The dataset exploited here is acquired from the previous study of Agius
74 et al. (2017). For this dataset, teleseismic P-to-S phase conversions were
75 obtained from permanent and temporary land and ocean bottom broadband
76 seismometers located across the Hawaiian archipelago (*e.g.* Hawaiian Plume-
77 Lithosphere Undersea Mantle Experiment – PLUME (Laske et al., 2009,
78 2011)). Preprocessing of the waveforms for ocean stations included removal
79 of the tilt noise on the vertical components (Crawford and Webb, 2000), re-
80 moval of the compliance noise (Bell et al., 2015), and reorientation of the
81 horizontal components. Both land and ocean stations were then band-pass
82 filtered between 0.05–0.2 Hz and had the horizontal components rotated to
83 the radial and transverse components. Waveforms of teleseismic earthquakes
84 with a magnitude greater than $M_w = 5.5$ and with an epicentral distance to
85 the stations between 35° and 80° were extracted for further analysis. Man-
86 ually selected P phases were deconvolved from the radial component using
87 the extended multitaper frequency domain deconvolution technique (Rychert
88 et al., 2013) to produce a receiver function. A positive amplitude receiver

89 function phase indicates a wave speed increase with depth, whereas a nega-
90 tive amplitude indicates a wave speed decrease.

91 Each receiver function was migrated to depth, and corrected for the
92 sphericity of the Earth. A one-dimensional, crust-corrected reference model
93 (PREM, (Dziewonski and Anderson, 1981; Leahy et al., 2010), Crust 1.0
94 (Laske et al., 2013)) was applied with additional corrections for the sta-
95 tions' elevations (Figure 1). Estimates for the uncertainties of the receiver
96 functions were determined with bootstrap resampling and averaging of the
97 receiver function traces within a bin. The migrated receiver functions were
98 then back-projected along the theoretical ray path and stacked onto a three-
99 dimensional (3-D) grid with a lateral spacing of 1° by 1° and a 1 km depth
100 vertical spacing. The grid is smoothed with a radius corresponding to the
101 Fresnel zone of the waveform (Figure 1). The depth and amplitude of the
102 positive peak close to the 410 and 660 km depth were selected as the mantle
103 transition zone discontinuities. Similarly, the depth and amplitude of the
104 negative peak atop the 410 were selected specifically for this study. Sporadic
105 positive polarity phases in the 200-350 km depth range in the model of Agius
106 et al. (2017), are likely related to small scale heterogeneity, as has frequently
107 been observed and described by other authors (*e.g.* Deuss, 2009). We also
108 observe phases within the transition zone similar to detections reported by
109 previous studies (Shearer, 1990). The standard error of the amplitudes and
110 of the discontinuity depths are shown in the supplementary material.

111 Based on this analysis of the dataset, we attempt to determine lateral
112 variations in the presence or absence of melt across the region. Such deter-
113 mination becomes achievable with our 3-D receiver function migration ap-

114 proach using a wide aperture array (Agius et al., 2017). Also note that our
115 inversion scheme fully accounts for and propagates errors quantitatively. Al-
116 though near-plume melt imaging is seemingly inconsistent with one previous
117 receiver function study that found no evidence for a melt layer above the 410
118 near plumes, the scale of our observation would not likely be resolvable by
119 the single station stack approach of the previous study (Tauzin et al., 2010).
120 We previously verified the robustness of interpreted transition-zone thick-
121 ness variations by implementing a variety of migrations models (Agius et al.,
122 2017). These models involve 1-D (PREM), 3-D with a central low shear wave
123 speed plume, and 3-D with a plume surrounded by fast shear wave speeds, af-
124 ter anomaly magnitudes reported by Wolfe et al. (2009). These tests showed
125 that the observed variability in transition zone thickness are robust.

126 *2.2. Rock physics analysis*

127 We carried out rock physics analysis using the numerical code MuMaP
128 (version 2.1, Hier-Majumder, 2020; Hier-Majumder et al., 2014). In this
129 method, we use two independent sets of seismic observations to constrain
130 the temperature and shear wave speed at each location. We then use the
131 mineral physics model of Xu et al. (2008) in combination with the calculated
132 temperature to isolate the effect of the bulk composition and temperature on
133 the seismic signature. Any residual negative anomalies are then attributed to
134 melting. In the following subsections, we describe these details in sequence.
135 Interested readers can see Hier-Majumder et al. (2014) for a more detailed
136 description of the analysis.

137 *2.2.1. Temperature*

138 The first step in our analysis involves calculating the temperature at
139 each of the 1681 locations of the dataset. We used two different methods
140 to estimate this temperature at each location (*i.e.*, in two separate sets of
141 rock physics inversions): (1) the thickness of the MTZ (Hier-majumder and
142 Tauzin, 2017; Tauzin and Ricard, 2014) and (2) the topography of the 410
143 km discontinuity (Hier-Majumder et al., 2014). On one hand, using the MTZ
144 thickness minimizes errors from unknown wave speed anomalies above 410
145 km depth, including in the crust, which may influence the seismically-inferred
146 depth of the 410 km (Tauzin and Ricard, 2014). On the other hand, using
147 the MTZ thickness as a proxy for temperature neglects any potential radial
148 temperature gradients across the MTZ.

149 To quantify the uncertainties arising from temperature, we computed
150 the temperature for 9 different Clapeyron slopes of the olivine-wadsleyite
151 transition in the range of 0.5 to 4.5 MPa/K for both sets of measurements.
152 Once the temperature anomalies are calculated, we convert these anomalies
153 to temperature by adding an adiabat with a specified potential temperature
154 and an adiabatic gradient of 0.3 K/km. To test the effects of potential
155 temperature, we carry out inversions for 5 different values of the potential
156 temperature ranging from 1127 to 1527 °C (1400–1800 K).

157 *2.2.2. Bulk solid composition*

158 In addition to temperature, we explore the effects of the excess fraction
159 of eclogite in the LVL mantle, f , on the resultant seismic wave speeds. In
160 our compositional model, the fraction f of the mantle consists of purely
161 basaltic component, while the rest, $1 - f$, consists of peridotite. We use the

162 compositional model from Xu et al. (2008), which suggests that the peridotite
163 consists of a mechanical mixture of 18% basalt and 82% harzburgite. The
164 bulk basalt fraction X , the quantity commonly used in the geophysics and
165 mineral-physics literature, and the excess eclogite fraction f , are then related
166 by

$$0.18(1 - f) + f = X, \quad (1)$$

167 where X is expressed as a fraction. In the inversions, we use X to evaluate
168 physical properties according to Xu et al. (2008). In the figures, we use f to
169 indicate the excess fraction of mantle eclogite. According to Sobolev et al.
170 (2007), the plume source material contains approximately 20% eclogite. In
171 the deep eclogitic pool (DEP) atop the transition zone (Ballmer et al., 2013),
172 discussed in Section 4, the solid matrix should be more enriched in eclogite
173 than the plume stem and is expected to have a higher value of f than 0.2.
174 We report the results for a conservative estimate of $f = 0.27$ ($X = 0.4$) for
175 the composition of the LVL matrix. As discussed in Section 3.2 in the region
176 around the plume stem, a higher value of f will lead to a higher predicted
177 median melt volume fraction than our conservative estimate. As a result,
178 our calculated LVL melt fractions remain a conservative estimate.

179 Once the temperature is evaluated at each point and a bulk solid com-
180 position is assigned to the mantle, we proceed to calculate the melt volume
181 fraction from the residual seismic anomaly, described next.

182 *2.2.3. Melting*

183 To calculate melt volume fractions, we start by defining a reference shear
184 wave speed, $V_S^{ref}(X, T)$ and an inferred shear wave speed, V_S^{inf} . The reference
185 shear wave speed is a theoretical value, dependent on the temperature (T)

186 and solid composition (X). Since we calculate the temperature at each point
 187 from either the MTZ thickness or the MTZ topography, this value is spatially
 188 variable. In contrast, we calculate the inferred shear wave speed from the
 189 normalized amplitude, R_{norm} , of the receiver function (Hier-Majumder et al.,
 190 2014). As the value of the normalized amplitude is spatially variable, so
 191 is V_S^{inf} . Notice, however, this spatial variation is independent of and, as
 192 shown later, generally different from the spatial variations in $V_S^{ref}(X, T)$.
 193 If, at a location, $V_S^{ref}(X, T) = V_S^{inf}$, no melting is necessary to explain
 194 the seismic observation. If, however, these two wave speeds are unequal
 195 and $V_S^{ref}(X, T) > V_S^{inf}$, we attribute the anomaly to melting. To quantify
 196 the amount of melting from the difference between these two independently
 197 derived wave speeds, we define a melt anomaly function, $\xi(\theta, \phi)$, such that

$$V_S^{inf} - \xi(\theta, \phi)V_S^{ref}(X, T) = \epsilon, \quad (2)$$

198 where $\epsilon \ll 1$ is the residual error of the calculation, θ is the solid-melt dihedral
 199 angle, and ϕ is the unknown melt-volume fraction. Using this definition, we
 200 can define the residual shear wave speed anomaly as (setting $\epsilon = 0$)

$$\Delta V_S = \frac{V_S^{inf} - V_S^{ref}}{V_S^{ref}} = \xi - 1. \quad (3)$$

201 Having incorporated the effects of temperature and bulk solid composition
 202 in computing V_S^{ref} , ΔV_S is independent from variations in temperature and
 203 solid composition within the parameter space of our inversion. Next, we
 204 invert the nonlinear, implicit equation (2) to calculate the unknown melt-
 205 volume fraction, ϕ , at each location.

206 *2.2.4. Parameter space*

207 To explore the parameter space, we carried out the inversions for 5 dif-
208 ferent values of mantle potential temperature, 7 dihedral angles between 10°
209 and 40°, 10 different values of X ranging from 0.1 to 0.99, and 9 different val-
210 ues of Clapeyron slope. All these analyses were carried out using 2 different
211 methods to evaluate lateral thermal anomalies in the transition zone (based
212 on either the MTZ thickness, or the topography of the 410-km discontinuity,
213 see above), totaling 6300 analyses for each of the 1681 data locations (or
214 more than 10 million inversions). Using this large parameter space not only
215 allows us to quantify the variations in calculated melt fractions, but also to
216 provide a robust estimate of the uncertainties arising from these variations,
217 discussed in section 2.3.

218 *2.2.5. Calculation of permeability and melt segregation velocity*

219 Once the melt fraction is evaluated at each point, we use the calculated
220 melt volume fraction to obtain the permeability and a zeroth order estimate
221 of melt migration velocity for the given melt fraction. We calculated the
222 permeability of melt from the melt fraction using a microstructural model of
223 melt in tubes at three-grain corners (Turcotte and Schubert, 2001, eq. 9-10).
224 ^{c1}In this model, the permeability, k , is related to the melt fraction, ϕ , by
225 the relation, $k = (b^2\phi^2) / 72\pi$, where $b = 1$ mm is the matrix grain size. To
226 evaluate the melt migration velocity, we use a 1D model of two-phase flow
227 and compaction (Bercovici et al., 2001; Hier-Majumder et al., 2006). In this
228 model, each point is treated as a melting column where the melt segregation

^{c1} *Authors: Text added.*

229 from the matrix is governed by compaction within the matrix and density-
230 driven segregation between the melt and the matrix. Following the method
231 outlined by Hier-Majumder and Courtier (2011), we solve the governing par-
232 tial differential analytically to obtain an expression for the melt segregation
233 velocity as a function of melt volume fraction within the column. For the
234 melt fraction at each location, we use the result of the rock physics inversion.
235 The interested reader is encouraged to see the details of this solution in the
236 work of Hier-Majumder and Courtier (2011).

237 *2.3. Calculation of uncertainties*

238 One of the strengths of our analysis is the identification of the first-order
239 uncertainties and quantification of the error in the calculated melt volume
240 fraction. We do not consider the putative influence of crystal-bound water
241 or melt composition in the reduction of seismic wave speeds. Recent exper-
242 imental results at LVL-like pressure temperature conditions show that the
243 influence of water on seismic wave speed reduction is small (Schulze et al.,
244 2018). In addition, there is a lack of documented systematic variation of
245 the wave speed in solids as a function of water related point defects in the
246 nominally anhydrous minerals under LVL-like conditions, precluding a pa-
247 rameter space search for uncertainty as carried out in this work. In two pre-
248 vious studies, Hier-Majumder et al. (2014) and Wimert and Hier-Majumder
249 (2012) experimented with the influence of melt composition on the calcu-
250 lations using equations of states of different melts. For small melt volume
251 fractions such as the LVL, the influence of melt composition was found to
252 be insignificantly small. In other words, we only focus on the factors that
253 exert a first-order influence on the calculated wave speed and are sufficiently

254 characterized, thus permitting a systematic parameter-space search.

255 We calculated the uncertainty in the melt volume fractions, α_ϕ , from the
256 uncertainties (α_i) in the four parameters (η_i): potential temperature (η_T),
257 basalt fraction (η_X), dihedral angle (η_θ), and the Clapeyron slope of olivine-
258 wadsleyite transformation (η_γ). The propagated error is calculated from the
259 uncertainties and gradients $\partial \langle \phi \rangle / \partial \eta_i$, using the formula

$$\alpha_\phi = \sqrt{\sum_i \alpha_i^2 \left(\frac{\partial \langle \phi \rangle}{\partial \eta_i} \right)^2_{j \neq i}} \quad (4)$$

260 where $\partial \langle \phi \rangle / \partial \eta_i$ is the rate of change of the median melt volume fraction with
261 changes in one of these four parameters, keeping the other three constant. We
262 use uncertainty values of $\alpha_\theta = \pm 5^\circ$ (Minarik and Watson, 1995), $\alpha_\gamma = \pm 0.8$
263 MPa/K (Tauzin and Ricard, 2014), and $\alpha_X = \pm 16\%$ (Sobolev et al., 2007)
264 and calculate the derivatives $\partial \langle \phi \rangle / \partial \eta_i$ numerically from our inversions. We
265 evaluate the uncertainty in temperature, α_T , from the standard deviation in
266 the measurement of the MTZ thickness, h_{MTZ} . For a mantle density of ρ ,
267 gravity, g , and a Clapeyron slope of γ , we estimate

$$\alpha_T = h_{MTZ} \frac{\rho g}{\gamma}. \quad (5)$$

268 Using $\rho = 3300 \text{ kg/m}^3$, $g = 10 \text{ ms}^{-2}$, $\gamma = 3 \text{ MPa/K}$, and $h_{MTZ} = 5.8 \text{ km}$
269 from our data, we get $\alpha_T = 63.8^\circ\text{C}$, which we use in equation 4. Inserting
270 these values in equation (4), we evaluate the error in melt volume fraction
271 $\alpha_\phi = \pm 0.3 \text{ vol}\%$.

272 3. Results

273 We carried out two sets of analyses—using two different methods for
274 determining temperature as described in Section 2.2.1—and found that dif-

275 ferences between the results are small. For example, the inferred median
276 melt-volume fractions calculated from these two methods differ only by ~ 0.01
277 vol%, an order of magnitude smaller than the propagated error. In this sec-
278 tion, we report temperatures calculated using our preferred method, MTZ
279 topography, unless stated otherwise.

280 *3.1. Melt distribution within the Hawaiian LVL*

281 The primary seismic observations and a few calculated quantities are
282 mapped in Figure 2. The MTZ beneath Hawaii (Figure 2(a), median thick-
283 ness 251 km) is characterized by a thin central region surrounded by a thicker,
284 concentric region. While such a feature is absent in the map of LVL thickness
285 in Figure 2(b), the thickest part of the LVL trends SE-NW, being elongated
286 roughly in the direction of plate motion. This correlation between LVL thick-
287 ness and plate motion suggests that the LVL is possibly a dynamic feature
288 interacting with the ambient mantle flow. We find that the temperature dis-
289 tribution near the 410 km discontinuity displays a bimodal spatial pattern.
290 Consistent with previous seismic P and S-wave tomography models (Wolfe
291 et al., 2009, 2011); the hot and seismically slow plume stem is surrounded by
292 a “halo” of cold and fast material (Figure 2(c)) (Agius et al., 2017).

293 The separation between the thermal and chemical component of the
294 Hawaiian LVL becomes clear from the map of the inferred and reference
295 seismic wave speeds. As expected, the map of reference wave speed, V_S^{ref} ,
296 (Figure 2(d)) closely follows the temperature distribution, with slow wave
297 speeds within the plume stem and fast wave speeds in the cold halo. Such a
298 halo is often interpreted as a curtain of cold downwelling from the base of the
299 lithosphere to the MTZ (Ballmer et al., 2013). In contrast to the tempera-

300 ture, the normalized amplitude of Ps conversions (Figure 2(e), median -0.88
301 (Agius et al., 2017)) displays a more diffuse spatial pattern. Indeed, the halo
302 is much less distinctive in the map of the inferred shear wave speed, V_S^{inf}
303 (Figure 2(f)). If variations in seismic properties were purely due to thermal
304 effects, V_S^{ref} and V_S^{inf} should be the same within the limit of uncertainties.
305 The difference between these two wave speed distributions, observed at this
306 resolution for the first time, highlights the separation between the thermal
307 and melting anomalies.

308 Our analysis shows that the patches which contain the highest melt frac-
309 tions lie outside the hot plume stem. The residual anomaly, ΔV_S , (Figure
310 3(a)) is mostly negative (median value of $-1.8 \pm 0.9\%$) within the LVL, imply-
311 ing the presence of partial melt. The melt distribution (median value of 0.4
312 $\pm 0.3\%$) closely follows the distribution of ΔV_S , as illustrated in Figure 3(b).
313 Parts of the LVL containing melt-volume fractions that exceed 1 vol% are
314 associated with the region between the plume stem and the halo (indicated
315 by isotherms in Figure 3(b)). In turn, the melt volume fraction is ≤ 0.5 vol%
316 within the plume stem (and even lower ^{c1} within the cold halo). This observa-
317 tion contradicts the expected spatial association between regions of high melt
318 volume fraction with regions of high temperatures, suggesting instead, that
319 the melt must have been carried away from the plume stem. The fact that
320 this melt displacement must be associated with mantle flow, is demonstrated
321 by a calculation of melt permeability and related buoyancy-driven melt-solid
322 segregation velocities (Figure s 3(c) and (d)). The relatively low inferred per-

^{c1} *Authors: than that*

323 meabilities ($\sim 10^{-14}\text{m}^2$) and melt-segregation velocities ($\sim 20 \mu\text{m}/\text{yr}$) suggest
324 that the $\sim 0.4 \text{ vol}\%$ melt in and near the plume stem are practically immobile
325 relative to the matrix, implying an important horizontal flow component of
326 the matrix.

327 3.2. The effect of Clapeyron slope, solid composition, and dihedral angle

328 Figure 4(a) shows the histogram for the calculated thermal anomalies for
329 three different values of the Clapeyron slope of olivine-wadsleyite transition.
330 ^{c1}An increase in the Clapeyron slope from 2 MPa/K to 4 MPa/K, leads to
331 a tighter probability distribution function centered around $\Delta T = 0$, with no
332 visible shift of the median value of the distribution. The maps in panels (b)
333 and (d) of Figure 4 show the calculated temperature anomaly distribution
334 for two different values of the Clapeyron slope. The primary influence of
335 the parameter Clapeyron slope is on the spread of the calculated thermal
336 anomaly. In turn, the median of inferred melt volumes remains virtually
337 unaffected by variations in Clapeyron slope (Figure 4(c)), ^{c2}since the cen-
338 tral tendency of the probability distribution in panel (a) is insensitive to the
339 variations in the Clapeyron slope.

340 In addition to the Clapeyron slope of the olivine-to-wadsleyite phase tran-
341 sition, we also explore the effects of the solid-melt dihedral angle for different
342 basalt fractions in the solid (Figure 5(a)). At higher dihedral angles, more
343 melt is confined to grain corners, resulting in a smaller fraction of wetted grain
344 boundaries. This leads to more effective intergranular contacts and stronger

^{c1} Authors: Text added.

^{c2} Authors: Text added.

345 skeletal networks of grains. To explain the calculated wave speed anomalies,
346 therefore, a larger melt volume fraction is required (Hier-Majumder, 2008;
347 Hier-Majumder and Abbott, 2010). But similar to the effects of recycled slab
348 component, discussed next, this trade-off does not change our main conclu-
349 sions.

350 Following the analysis of single crystals in Hawaiian lavas, Sobolev et al.
351 (2007, 2005) estimated that the Hawaiian plume source contains approxi-
352 mately 20% recycled slab component in addition to pyrolite. This basaltic
353 component may ^{c1} be filtered near the top of the MTZ due to mechanical
354 sequestration into a deep eclogitic pool (Ballmer et al., 2013; Cheng et al.,
355 2015). Such a sequestration is promoted by a maximum of the negative den-
356 sity anomaly of (silica-normative) basaltic materials in the depth range of
357 about 300-410 km depth (Aoki and Takahashi, 2004). ^{c2}The mechanical se-
358 questration of basalt-rich matrix into the deep eclogitic pool occurs by lateral
359 spreading of this neutrally buoyant matrix just beneath the depth of den-
360 sity inversion (Ballmer et al., 2013). The extent of the related segregation
361 of basalt from the rest of the mantle, however, remains poorly constrained.
362 While the lower limit of eclogite fraction f in the LVL is 20% (*i.e.* no segre-
363 gation), the upper limit may be much higher. In this work, we report results
364 for $f = 27\%$, *i.e.* near the lower bound.

365 Here, we quantify the effect of variable basalt fraction in the solid on
366 the calculated melt-volume fractions (Figure 5, also see Figure 4(c)). We
367 find that the reference wave speed increases with increasing f , well explained

^{c1} *Authors: Text added.*

^{c2} *Authors: Text added.*

368 by the higher elastic moduli of eclogite compared to pyrolite. Accordingly,
369 more melt is required for higher f in order to explain the observed residual
370 shear wave speed anomalies. In turn, smaller basalt contents yield smaller
371 inferred melt fractions. Nevertheless, finite melt fractions in the LVL of a
372 similar order of magnitude are always required for $f \geq 20\%$. Thus, our main
373 conclusions remain robust independent of f . As shown in Figure 5, the same
374 statement is true for the combined effects of f and solid-melt dihedral angle.

375 The maps in Figure 5(c) depict the distribution of melt vol% for four
376 different ^{c1}volume fractions of f . As shown in the maps, with increasing f ,
377 the calculated melt volume fractions show an overall increase, but the pattern
378 of melt distribution remains virtually unaffected. The most melt-rich region
379 occurs to the east of the hot plume stem, near the 1580°C isotherm. Note
380 that any finite melt fractions imply significant volatile fluxes to the LVL,
381 due to the strongly incompatible behavior of H₂O and CO₂ (Aubaud, 2004;
382 Hirschmann and Dasgupta, 2009).

383 3.3. *The relationship between temperature and LVL thickness*

384 An important outcome of our analysis is that the thickness and internal
385 structure of the LVL is clearly distinct from the temperature field inferred
386 from MTZ thickness. As shown in Figure 6(a), there is no visible corre-
387 lation between LVL thickness and temperature. In Figure 6(b), we plot
388 the unprocessed amplitude of Ps conversion as a function of the calculated
389 melt fractions. As the color of the symbols indicate, for a given measured

^{c1} *Authors: values*

^{c2} *Authors: Text added.*

390 amplitude, variations in melt fraction arise from variations in temperature,
391 as their effects trade-off with each other. Once the effects of temperature
392 are corrected for by subtracting the reference wave speed V_S^{ref} , the resid-
393 ual anomaly only depends on melt fraction (Figure 6(d)). The color of the
394 points in Figure 6(c) show that higher melt fractions, up to 1.7 vol%, are
395 associated with larger negative ΔV_S . Ultimately, the residual ΔV_S and the
396 inferred melt fractions are not strongly controlled by temperature (*i.e.*, no
397 correlation), consistent with our interpretation of volatile-assisted melting.

398 3.4. Results from temperature calculations using 410 km topography

399 The maps in Figure 7 show the results of our inversion for melt content
400 using the topography of the 410-km discontinuity to determine temperature,
401 *i.e.* instead of MTZ topography. These calculations were carried out for
402 a potential temperature of 1427°C, bulk excess eclogite fraction of 27%, a
403 dihedral angle of 25°, and a Clapeyron slope of olivine to wadsleyite tran-
404 sition of 3 MPa/K. The median melt volume fraction for this calculation is
405 0.3 vol%, similar to that obtained by using the MTZ thickness as a proxy
406 for temperature. As the maps indicate, the plume stem appears wider and
407 the cold ‘halo’ is substantially reduced in this approach compared to that
408 shown in ^{c1} ^{c2}[Figure 2](#). As shown by the work of Tauzin and Ricard (2014),
409 crustal effects above plumes can lead to overestimation of 410 km depth and
410 introduce errors in the inferred temperature. Using the thickness of MTZ as
411 a proxy eliminates this source of error. While we prefer the temperatures

^{c1} Authors: ~~the main article~~

^{c2} Authors: Text added.

412 that are calculated from MTZ thickness, some earlier publications used 410-
413 km topography as a proxy for temperature. Thus, we include this result for
414 reference here.

415 **4. Plume leakage and volatile fluxes**

416 The separation between thermal and chemical signatures provides us with
417 an indication of the geodynamic processes operative within the Hawaiian
418 LVL. Based on our seismic observations and calculated melt volume fractions,
419 two distinct patterns of flow within the LVL can be discerned when the map
420 of temperature in Figure 2(c) is compared with the map of melt distribution
421 in 3(b) (also the cartoon in 8(a)). Dominantly vertical up and downwelling
422 flows, driven by thermal buoyancy, are consistent with the inferred thermal
423 structure in Figure 2(c). In turn, practically immobile melt fractions—^{c1}evi-
424 denced by an average melt percolation speed of 22 $\mu\text{m}/\text{yr}$ within and near the
425 plume conduit ^{c2}(Figure 3(d))—indicate a second, dominantly horizontal flow
426 of the plume matrix. Such spreading and stagnation of a “thermochemical”
427 plume, which contains a significant fraction of basaltic material in addition
428 to peridotite (Sobolev et al., 2007), can be caused by a sharp decrease of the
429 buoyancy of basaltic material just above 410 km depth (Aoki and Takahashi,
430 2004; Ballmer et al., 2013). Spreading and pooling of eclogitic material at the
431 periphery of the Hawaiian plume at these depths is consistent with regional
432 seismic tomography (Cheng et al., 2015), and provides a mechanism for the
433 long-term stabilization of melts away from the plume stem. As the incipient

^{c1} *Authors: Text added.*

^{c2} *Authors: Text added.*

434 melt is dragged away from the hot plume stem, it does not freeze, because
435 the pooling eclogitic material remains warm (Ballmer et al., 2013), and hence
436 well above the volatile-rich solidi (Figure 8(b)). Comparison between the
437 carbonated basalt (Thomson et al., 2016) and hydrous peridotite (Ohtani
438 et al., 2004) solidi and our inferred temperatures (*i.e.*, 1440-1640°C; Figure
439 8(b)) illustrates that the observed melts must be generated by volatiles in
440 the plume. It is important to notice that our melt fraction calculations were
441 not constrained by any solidus, the coincidence of the seismically derived
442 temperature and pressure and the solidi is thus completely independent of
443 the rock physics analysis.

444 The leakage of melt from the Hawaiian plume leads to a substantial
445 volatile flux back into the mantle. These lost volatiles may never reach the
446 uppermost mantle, or even the atmosphere. Due to the strongly incompatible
447 nature of H₂O (Aubaud, 2004) and CO₂ (Hirschmann and Dasgupta, 2009),
448 the observed 0.4 vol% partial melt can store 3.7 wt% H₂O and 5.5 wt% CO₂
449 (see Appendix A), substantially higher than the measured concentrations of
450 these volatiles in olivine-hosted melt inclusions from Hawaiian lavas (Hauri,
451 2002). Using our observed LVL thicknesses and melt-volume fractions, as
452 well as published partition coefficients and volatile abundances in the plume
453 source, we estimate that the Hawaiian plume can leak between 0.7 and 10.7
454 Mt/yr of CO₂ and between 0.6 and 1.9 Mt/yr of H₂O to the LVL. For com-
455 parison, the present day CO₂ surface flux at Kilauea volcano is measured
456 at 2.4 Mt/yr (Burton et al., 2013). Given the observed global correlations
457 between plumes and LVLs (Vinnik and Farra, 2007), and this estimated loss
458 to the LVL, the global CO₂ flux carried by plumes —before they enter the

459 MTZ— needs to be significantly higher than the estimated 4-110 Mt/yr of
460 CO₂ outgassed at hotspots (Dasgupta and Hirschmann, 2010). Similarly, sig-
461 nificant amounts of H₂O carried by mantle upwellings may never reach the
462 surface. These estimated fluxes demonstrate that LVLs act as gatekeepers
463 for mantle volatiles, but are currently neglected in models of global volatile
464 cycles (Dasgupta and Hirschmann, 2010; Kelemen and Manning, 2015; Plank
465 and Manning, 2019). Additionally, the higher incompatibility of CO₂ rela-
466 tive to H₂O (Aubaud, 2004; Hirschmann and Dasgupta, 2009), coupled with
467 the small degree of melting, will tend to preferentially sequester the former
468 into the LVL and back into the deep mantle (Hirschmann and Dasgupta,
469 2009). Such carbon enrichment of the LVL and deep mantle, a reservoir that
470 has previously not been accounted for, can explain some or all of the miss-
471 ing mantle carbon, reconciling the seemingly discrepant observation of lower
472 C:H ratio in the known mantle reservoirs compared to chondritic meteorites
473 (Hirschmann and Dasgupta, 2009). Further constraints on the global leak-
474 age of volatiles at mantle plumes may advance our understanding of volatile
475 delivery to Earth, and across the early solar system.

476 ^{c1}

477 5. Conclusions

478 In this study, our rock physics analysis of teleseismic P-to-S conversions
479 reveal the internal structure and melt distribution of the LVL above the
480 Hawaiian MTZ. The key conclusions of this study are:

^{c1} *Authors: Text added.*

- 481 • The Hawaiian LVL is characterized by patches containing up to 1.7
482 vol% melt outside the hot plume stem, while the regional melt distri-
483 bution has a median of 0.4 ± 0.3 vol%.
- 484 • The small melt volume fraction in the LVL, owing to reduced perme-
485 ability, leads to a median melt segregation velocity of ~ 20 $\mu\text{m}/\text{year}$,
486 effectively trapping the melt within the matrix.
- 487 • The location of high melt concentration, coupled with low melt mobil-
488 ity, suggests a possible lateral transport or leakage of matrix-trapped
489 melt, away from the plume stem.
- 490 • Based on published petrological and geochemical data, we infer that
491 the Hawaiian plume can leak up to 1.9 Mt/yr H_2O and 10.7 Mt/yr CO_2
492 to the LVL.

493 **Acknowledgment**

494 C.A.R. and N.H. acknowledge funding from the Natural Environment
495 Research Council (NE/M003507/1 and NE/K010654/1) and the European
496 Research Council (GA 638665). SH-M acknowledges support from National
497 Science Foundation, USA (EAR 1215800). The inversions on MuMaP were
498 carried out on ARCHER.

499 **Appendix A. Calculation of volatile fluxes**

500 Based on our calculation of melt-migration velocities, which remain very
501 small, we infer that the volatiles are carried away from the plume stem via im-
502 mobile melt trapped in the triple grain junctions, i.e. by a laterally-spreading

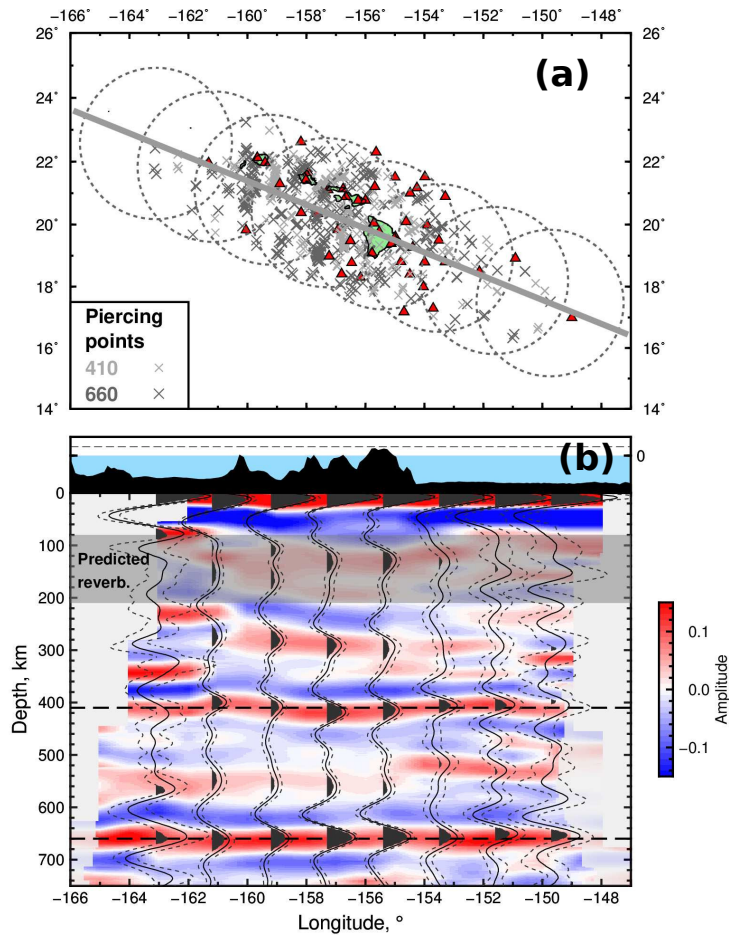


Figure 1: ^{c3}(a) The gray line across the map shows the location of the vertical cross section shown in the panel below. Red triangles are the seismic stations used for the bootstrap. Crosses are the corresponding piercing points at 410- and 660-km depth. (b) Vertical cross-sections through the 3-D depth migrated receiver functions calculated using a crust-corrected PREM wave speed model (Dziewonski and Anderson, 1981). Red and blue shades represent positive and negative amplitudes saturated at ± 0.15 , respectively. The image resolution is from a 1° by 1° latitude-longitude grid. Semi-transparent shades represent poorly constrained areas due to a low number of traces (< 5). Black solid wiggles represent the stacked bin average for the respective area shown on the map above (dashed circles). ^{c4} Dashed wiggles are two standard deviations estimated from bootstrap analysis using 100 randomly selected subsets from within the respective bins. Gray shaded band indicates predicted crustal reverberations. 2

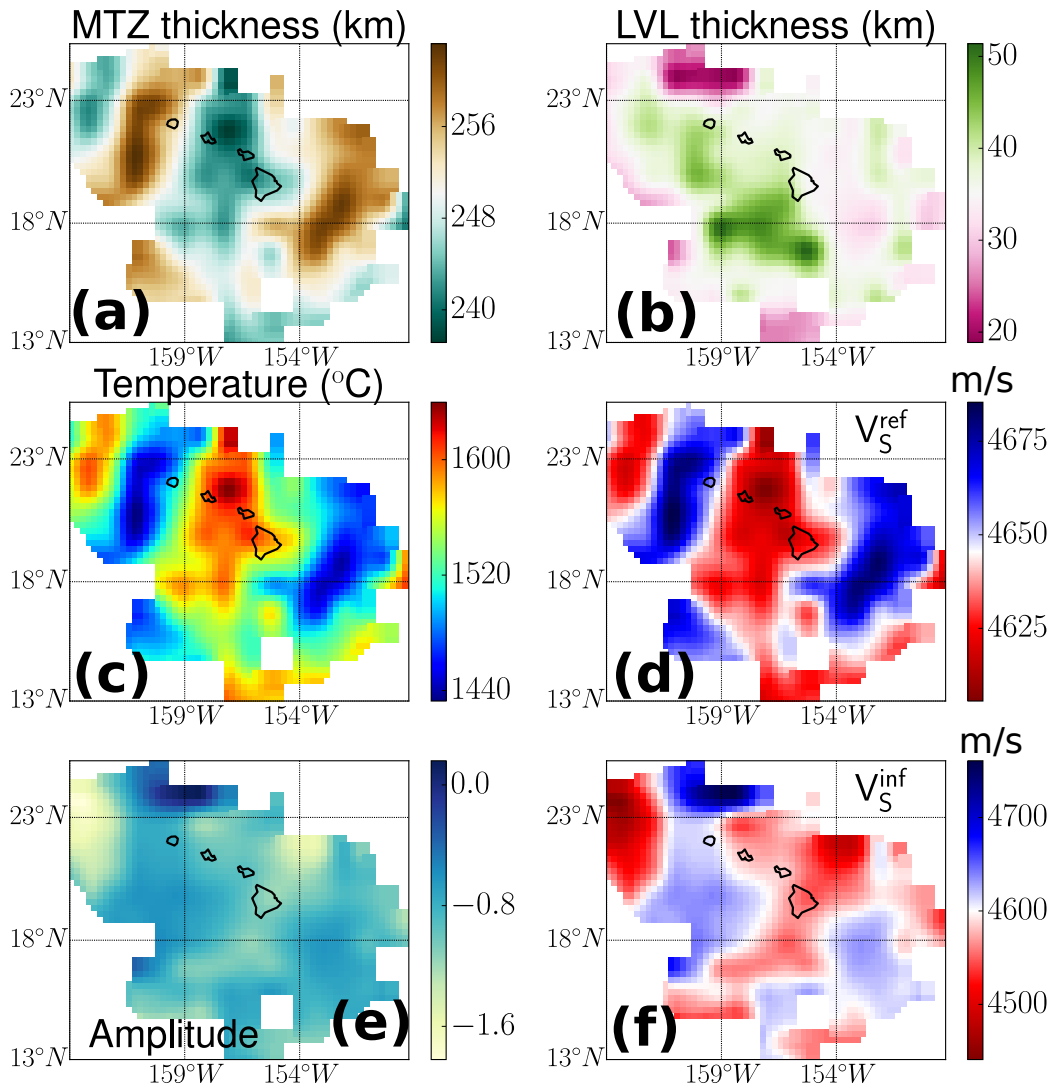


Figure 2: Map of the thermochemical anomalies above the transition zone. (a) Transition zone thickness measured from the Ps conversions. (b) Thickness of the LVL, measured by the distance between the LVL and the top of the MTZ using receiver functions (Agius et al., 2017). (c) The temperature at each point is calculated from the observed transition zone thickness for a mantle potential temperature of 1700 K and a Clapeyron slope for Olivine-Wadsleyite transition of 3 MPa/K. (d) Reference mantle wave speed calculated from the temperature at each point for a mantle eclogite fraction of 27%. (e) The observed amplitude of Ps conversion at the LVL normalized by the amplitude change atop the 410 km discontinuity. (f) The magnitude of shear wave speed calculated from the observed amplitude. (Hier-Majumder et al., 2014).

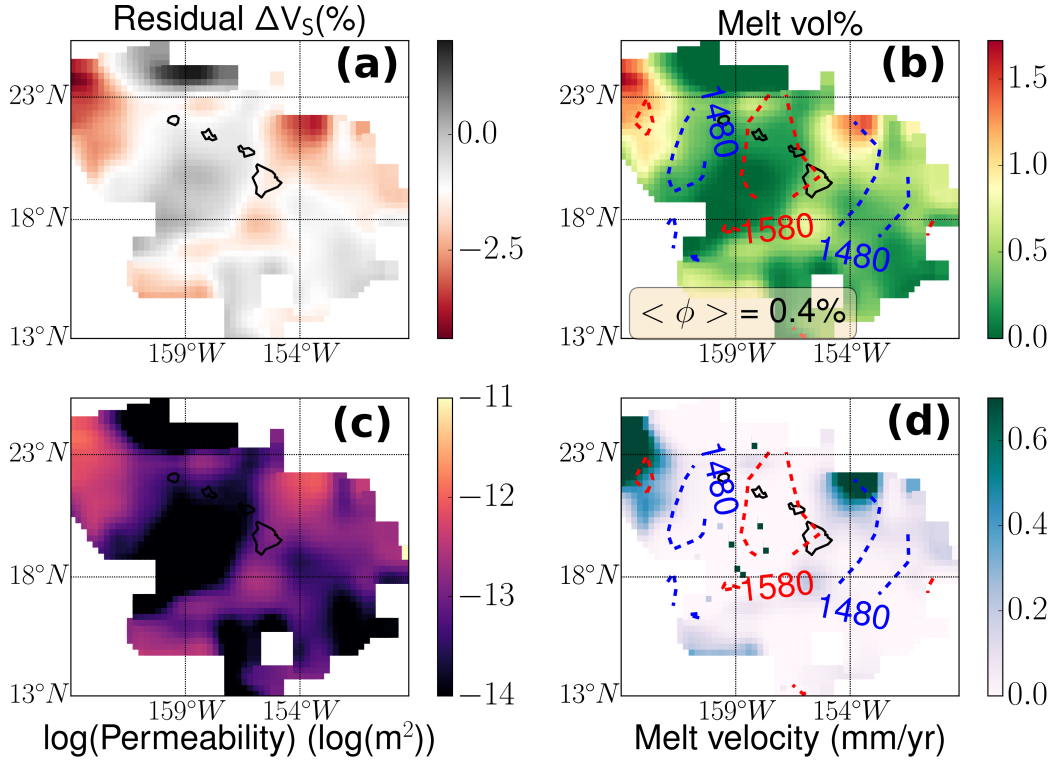


Figure 3: Melt distribution and flow, inferred from the normalized residual wave speed anomaly ΔV_S . (a) Map of ΔV_S , as calculated from V_S^{ref} and V_S^{inf} . (b) Map of melt volume fraction, as calculated from ΔV_S , using a dihedral angle of 25° at the melt grain interface. (c) Map of melt permeability, as calculated from the melt volume fraction at each point using a model of melt tubules along triple grain junctions. The median value of the permeability is $6.0 \times 10^{-14} \text{ m}^2$ (d) Buoyancy-driven segregation velocity of melt in a 1D compacting column, as calculated from an analytical solution of the compaction equations (Hier-Majumder and Courtier, 2011). The median value of the velocity is $22 \text{ } \mu\text{m}/\text{yr}$.

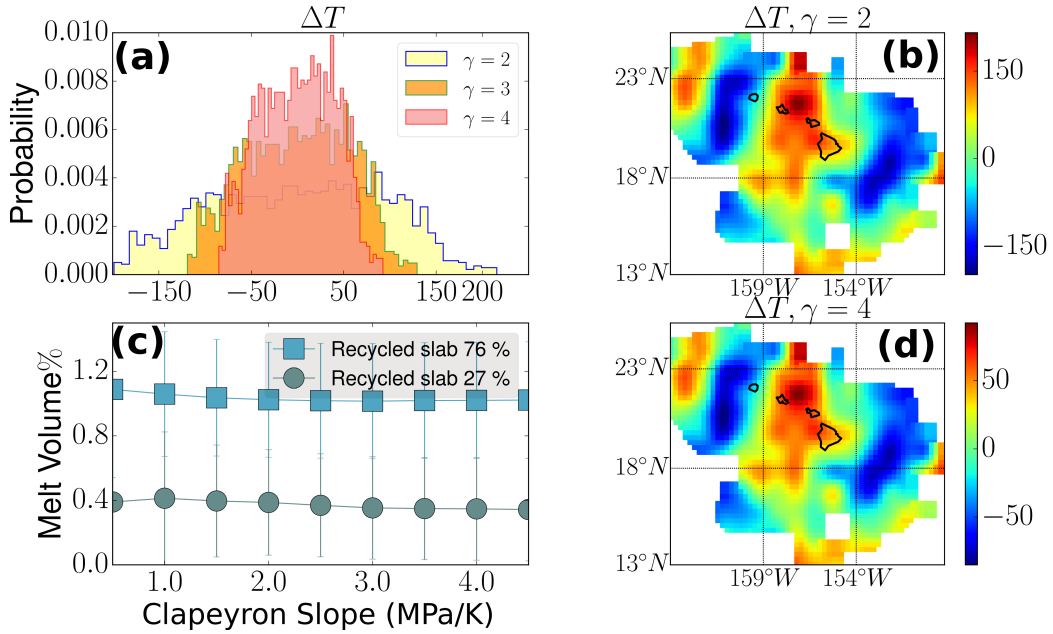


Figure 4: (a) Histogram showing the probability distribution of calculated temperature anomalies for three different values of Clapeyron slope (γ) of the olivine-wadsleyite transition. Maps of the temperature anomalies for (b) $\gamma = 2$ and (c) $\gamma = 4$. In Figure 4(c), the potential temperature has a constant value of 1700 K. (d) Plot of calculated median melt volume fraction as a function of the Clapeyron slope γ , used to calculate the temperature. Two series of data plots are shown for two different basalt fractions in the bulk composition.

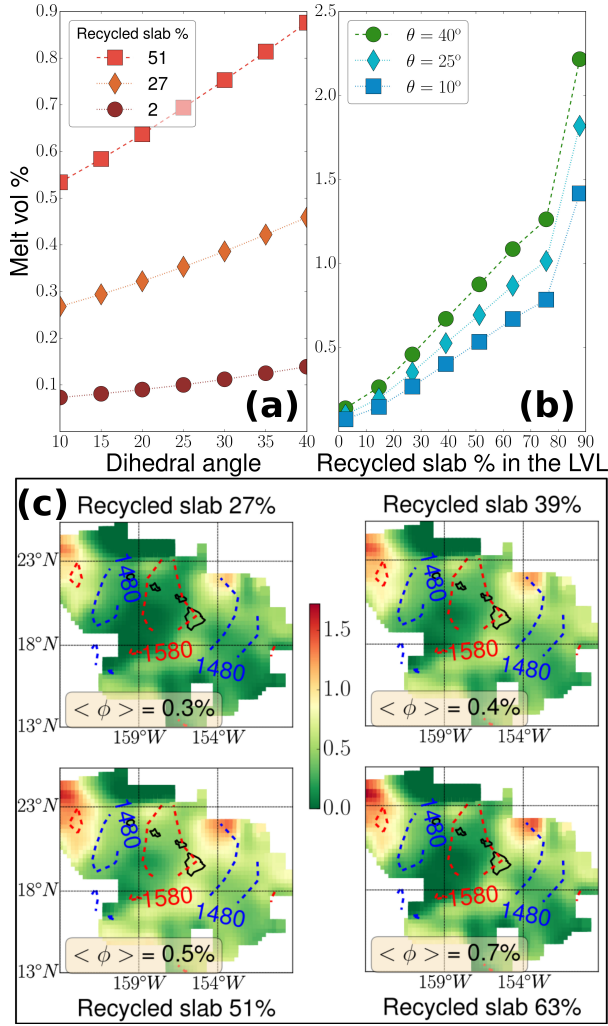


Figure 5: Plot of calculated median melt volume fraction as a function of (a) dihedral angle (θ) (b) and bulk composition (fraction of recycled slab in the mantle, f). (c) Maps of melt volume % for four different values of f . Potential temperature is 1700 K and the dihedral angle is 25° . The value of median melt vol%, $\langle \phi \rangle$ for each map is shown in the inset.

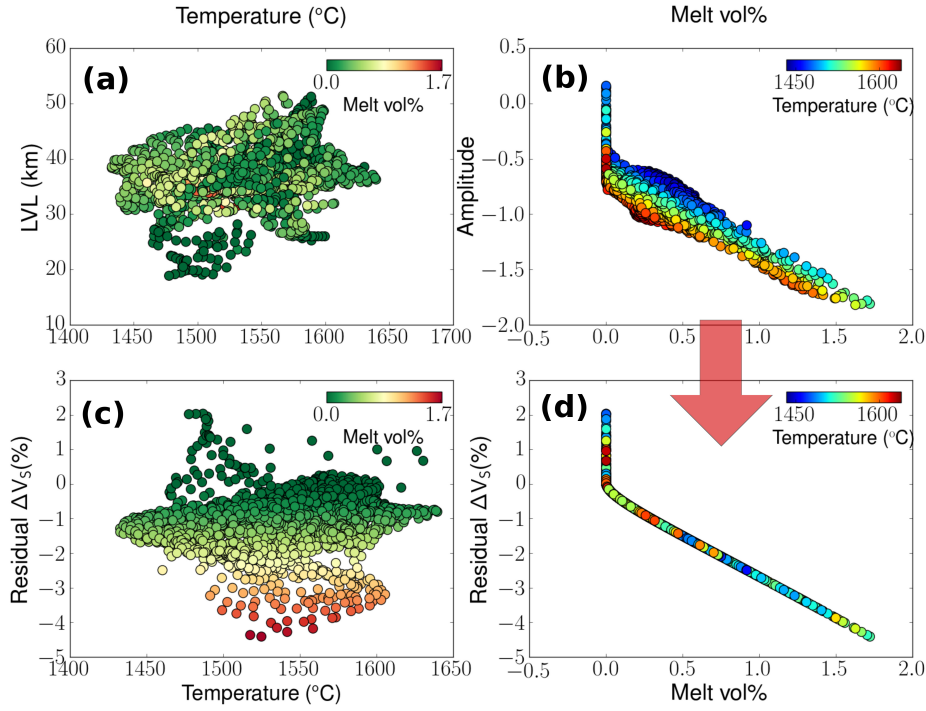


Figure 6: (a) Scatter plot of LVL thickness as a function of the calculated temperature for all data points in this study. The data points are colored by the melt volume fraction calculated at each location. (b) Plot of normalized P-S conversion amplitude as a function of calculated melt volume% at each location in the region. The data points are colored by the temperature at each location. ^{c8} ^{c9}(c) Scatter plot of temperature and the residual shear wave speed ΔV_S . The data points are colored by the melt volume fraction. (d) The residual wave speed anomaly as a function of calculated melt volume%. The data points are colored by the temperature at each location. Spread in the observed amplitude is removed by the thermal correction indicated by the arrow between panels (b) and (d). ^{c10}

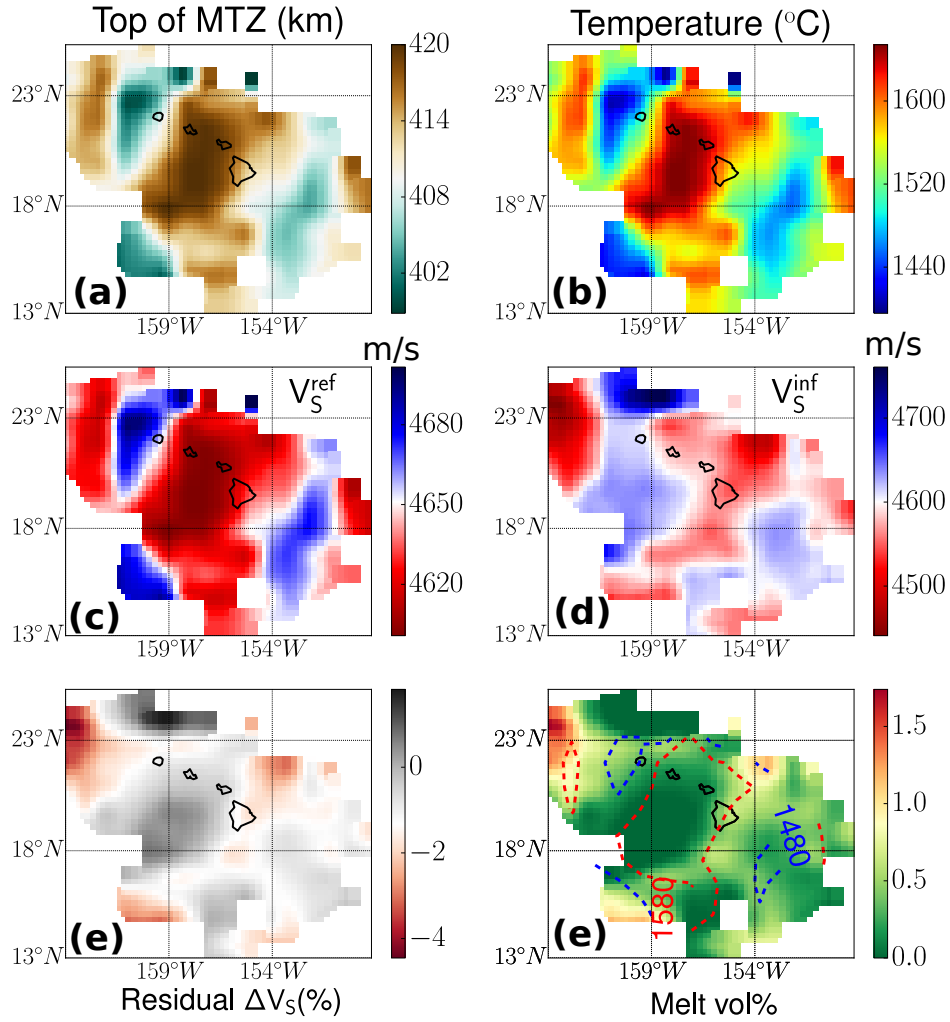


Figure 7: Map of analysis results using the 410 km topography (top of MTZ) to calculate the temperature. (a) Top of the MTZ shown in km. (b) Temperature calculated from the 410 km topography, (c) reference wave speed, (d) inferred wave speed, (e) residual ΔV_s and (f) map of the calculated melt volume% with two isotherms overlain. For these maps, the other parameters are identical to that in Figures 1 and 2 of the main article.

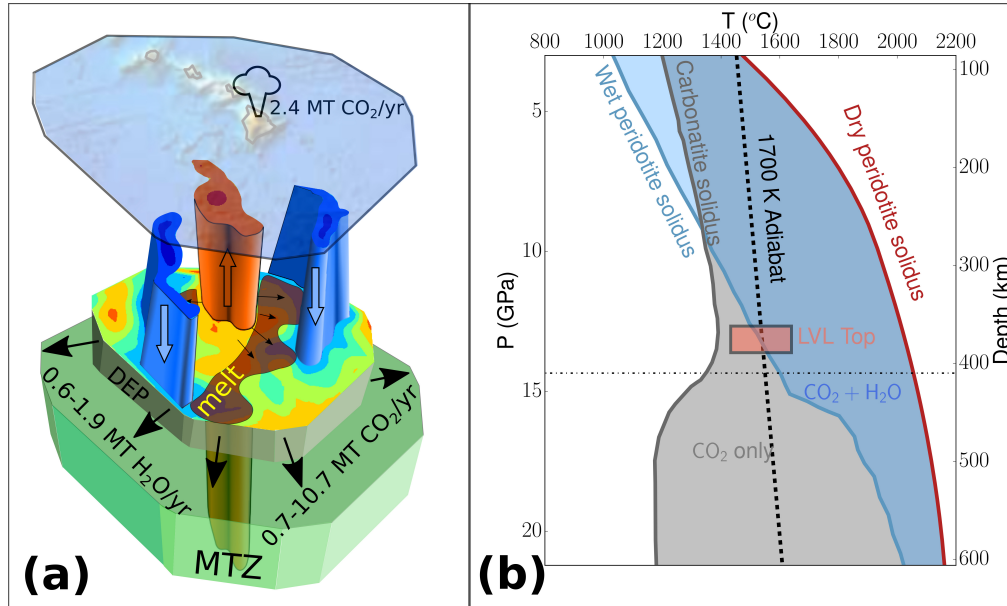


Figure 8: Mantle motion, volatile fluxes, and melting curves for the Hawaiian LVL. (a) A schematic diagram outlining melt leakage around the plume stem aided by lateral flow of a stagnated, spreading deep eclogite pool (DEP) atop the MTZ. The melt-rich regions are shaded in dark brownish red. (b) Solidi of carbonatite (Thomson et al., 2016) and hydrous peridotite (Ohtani et al., 2004) compared with the 1700 K adiabat. Width of the horizontal box corresponds to the range of temperature inferred from the transition zone thickness for the same adiabat. The vertical extent of the box depicts the range of LVL thicknesses inferred in this study.

503 flow of the mantle matrix rather than melt percolation through the matrix.

504 ^{c11}In this section, we present a zeroth order calculation of the flux of volatiles
505 associated with the lateral spreading. Our calculations make a few simpli-
506 fying assumptions, such as uniform leakage of melt around the plume stem
507 and volatile concentration within the plume stem is equal to the source con-
508 centration. While a detailed model of volatile leakage—capturing these com-
509 plexities of the flow—is outside the scope of this article, the magnitude of
510 volatile fluxes calculated by this simple approach highlights the importance
511 of this flux, currently ignored in global carbon cycle models.

512 ^{c1}With the caveat mentioned above, we derive the simple equation to cal-
513 culate the volatile flux. Assuming a horizontal mantle flow velocity of v , and
514 an LVL thickness of h , the total volume flow per unit time across the vertical
515 boundary of a cylindrical plume stem is given by $2\pi r h v$, where r is the radius
516 of the plume. If the melt volume fraction is given by ϕ , and the melt density
517 by ρ_m , then the melt flow per unit time is $2\pi r h v \phi \rho_m$. Finally, for a volatile
518 concentration of c in the melt, the mass flow rate of the volatile is given by,
519 $2\pi r h v \phi \rho_m c$.

520 While we do not have a direct way of measuring the concentration of
521 volatiles in the melt, we can use the estimates of the volatile concentration
522 near the center of the plume stem. If this source concentration is given as c_0 ,
523 and the partition coefficient of the volatile is given by $D^{solid/melt}$, then using

^{c11} *Authors: Text added.*

^{c1} *Authors: Text added.*

524 the batch melting model, we get,

$$c = \frac{c_0}{(1 - D)\phi + D}. \quad (\text{A.1})$$

525 Using published values of $D^{\text{solid/melt}}$, we can calculate the concentration of
526 CO₂ and H₂O in the LVL. For example, for $D_C^{\text{solid/melt}} = 0.001$ (Hirschmann
527 and Dasgupta, 2009), $D_H^{\text{solid/melt}} = 0.009$ (Aubaud, 2004), source concentra-
528 tions of CO₂ = 250 ppm (Anderson and Poland, 2017) and H₂O = 450 ppm
529 (Bizimis and Peslier, 2015), and our median melt volume fraction of 0.0035,
530 we get 5.5 wt% CO₂ and 3.7 wt% H₂O in the LVL. Next, we can use this
531 formula to calculate the fluxes of each of these volatiles away from the plume,

$$F = 2\pi r h v \phi \rho_m \left[\frac{c_0}{(1 - D)\phi + D} \right]. \quad (\text{A.2})$$

532 We use the median values of LVL thickness, $h = 35$ km, and melt volume
533 fraction, $\phi = 0.0035$, from this study, $\rho_m = 3400\text{kg/m}^3$ (Ghosh et al., 2007),
534 $v = 10$ cm/yr (Ballmer et al., 2013), and $r = 100$ km. To estimate the upper
535 and lower bounds of CO₂ and H₂O fluxes, we use the estimates of $c_0 = 120$ -
536 1830 ppm CO₂ and $c_0 = 300$ -900 ppm H₂O in the OIB source (Hirschmann
537 and Dasgupta, 2009). These values lead to the flux ranges of 0.7 to 10.7
538 Mt/yr of CO₂ and 0.6 to 1.9 Mt/yr of H₂O, respectively.

539 **References**

- 540 Agius, M. R., Rychert, C. A., Harmon, N., Laske, G., 2017. Mapping the
541 mantle transition zone beneath Hawaii from Ps receiver functions : Evi-
542 dence for a hot plume and cold mantle downwellings. *Earth and Planetary*
543 *Science Letters* 474, 226–236.
- 544 Anderson, K. R., Poland, M. P., 2017. Abundant carbon in the mantle be-
545 neath Hawai'i. *Nature Geoscience* 10 (9), 704–708.
- 546 Aoki, I., Takahashi, E., 2004. Density of MORB eclogite in the upper mantle.
547 *Physics of the Earth and Planetary Interiors* 143 (1-2), 129–143.
- 548 Aubaud, C., 2004. Hydrogen partition coefficients between nominally anhy-
549 drous minerals and basaltic melts. *Geophysical Research Letters* 31 (20),
550 2–5.
- 551 Ballmer, M. D., Ito, G., Wolfe, C. J., Solomon, S. C., 2013. Double layering
552 of a thermochemical plume in the upper mantle beneath Hawaii. *Earth*
553 *Planet. Sci. Lett.* 376, 155–164.
- 554 Bell, S. W., Forsyth, D. W., Ruan, Y., 2015. Removing noise from the vertical
555 component records of ocean-bottom seismometers: Results from year one
556 of the cascadia initiative. *Bulletin of the Seismological Society of America*
557 105 (1), 300–313.
- 558 Bercovici, D., Karato, S., 2003. Whole-mantle convection and the transition
559 zone water filter. *Nature* 425, 39–44.

- 560 Bercovici, D., Ricard, Y., Schubert, G., 2001. A two-phase model for com-
561 paction and damage; 1, General theory. *Journal of Geophysical Research*,
562 B, Solid Earth and Planets 106 (5), 8887–8906.
- 563 Bizimis, M., Peslier, A. H., 2015. Water in Hawaiian garnet pyroxenites:
564 Implications for water heterogeneity in the mantle. *Chemical Geology* 397,
565 61–75.
- 566 Burton, M. R., Sawyer, G. M., Granieri, D., 2013. Deep Carbon Emissions
567 from Volcanoes. *Reviews in Mineralogy and Geochemistry* 75 (1), 323–354.
- 568 Cheng, C., Allen, R. M., Porritt, R. W., Ballmer, M. D., 2015. Seismic Con-
569 straints on a Double-Layered Asymmetric Whole-Mantle Plume Beneath
570 Hawai'i. In: Carey, R and Cayol, V and Poland, M and Weis, D (Ed.),
571 HAWAIIAN VOLCANOES: FROM SOURCE TO SURFACE. Vol. 208 of
572 Geophysical Monograph Book Series. Amer Geophys Union, pp. 19–34.
- 573 Crawford, W. C., Webb, S. C., 2000. Identifying and Removing TiltNoise
574 from Low Frequency LT0.1Hz Seafloor Vertical Seismic Data. *Bulletin of*
575 *the Seismological Society of America* 90 (4), 952–963.
- 576 Dasgupta, R., Hirschmann, M. M., 2010. The deep carbon cycle and melting
577 in Earth's interior. *Earth Planet Sci. Lett* 298, 1–13.
- 578 Deuss, A. ., 2009. Global observations of mantle discontinuities using ss and
579 pp precursors. *Surv. Geophys.* 30, 301–32.
- 580 Dziewonski, A. M., Anderson, D. L., 1981. Preliminary reference Earth
581 model. *Physics of the Earth and Planetary Interiors* 25 (4), 297–356.

- 582 Ghosh, S., Ohtani, E., Litasov, K., Suzuki, A., Sakamaki, T., NOV 22 2007.
583 Stability of carbonated magmas at the base of the Earth's upper mantle.
584 GEOPHYSICAL RESEARCH LETTERS 34 (22).
- 585 Hauri, E., 2002. SIMS analysis of volatiles in silicate glasses, 2: Isotopes
586 and abundances in Hawaiian melt inclusions. *Chemical Geology* 183 (1-4),
587 115–141.
- 588 Hier-Majumder, S., DEC 11 2008. Influence of contiguity on seismic veloci-
589 ties of partially molten aggregates. *Journal of Geophysical Research-Solid*
590 *Earth* 113 (B12), B12205.
- 591 Hier-Majumder, S., Feb. 2020. sashgeophysics/mumap: Mumap v2.1.
592 URL <https://doi.org/10.5281/zenodo.3673226>
- 593 Hier-Majumder, S., Abbott, M. E., OCT 15 2010. Influence of dihedral angle
594 on the seismic velocities in partially molten rocks. *Earth and Planetary*
595 *Science Letters* 299 (1-2), 23–32.
- 596 Hier-Majumder, S., Courtier, A., 2011. Seismic signature of small melt frac-
597 tion atop the transition zone. *Earth and Planetary Science Letters* 308 (3-
598 4), 334–342.
- 599 Hier-Majumder, S., Keel, E., Courtier, A., 2014. The influence of tempera-
600 ture, bulk composition, and melting on the seismic signature of the low
601 velocity layer above the transition zone. *J. of Geophys. Res. Solid Earth*
602 119.
- 603 Hier-Majumder, S., Ricard, Y., Bercovici, D., AUG 30 2006. Role of grain

604 boundaries in magma migration and storage. *Earth and Planetary Science*
605 *Letters* 248 (3-4), 735–749.

606 Hier-majumder, S., Tauzin, B., 2017. Pervasive upper mantle melting be-
607 neath the western US. *Earth and Planetary Science Letters* 463, 25–35.

608 Hirschmann, M. M., Dasgupta, R., May 2009. The H/C ratios of Earth’s
609 near-surface and deep reservoirs, and consequences for deep Earth volatile
610 cycles. *Chemical Geology* 262 (1-2), 4–16.

611 Kelemen, P. B., Manning, C. E., 2015. Reevaluating carbon fluxes in subduc-
612 tion zones, what goes down, mostly comes up. *Proceedings of the National*
613 *Academy of Sciences* 112 (30), E3997–E4006.

614 Kohlstedt, D., Keppler, H., Rubie, D., 1996. Solubility of water in the α , β
615 and γ phases of $(\text{Mg, Fe})_2\text{SiO}_4$. *Contributions to Mineralogy and Petrology*
616 123, 345–357.

617 Laske, G., Collins, J. A., Wolfe, C., Solomon, S., Detrick, R.S.and Orcutt,
618 J. B. D., Hauri, E., 2009. Probing the hawaiian hot spot with new ocean
619 bottom instruments. *EOS, Trans. Am. geophys. Un.* 90, 362–3.

620 Laske, G., Markee, A., Orcutt, J. A., Wolfe, C. J., Collins, J. A., Solomon,
621 S. C., Detrick, R. S., Bercovici, D., Hauri, E. H., 2011. Asymmetric shal-
622 low mantle structure beneath the Hawaiian Swell-evidence from Rayleigh
623 waves recorded by the PLUME network. *Geophysical Journal International*
624 187 (3), 1725–1742.

625 Laske, G., Masters, G.and Ma, Z., Pasyanos, M., 2013. Update on crust1.0 -
626 a 1-degree global model of earths crust. p. 2658.

- 627 Leahy, G. M., Collins, J. A., Wolfe, C. J., Laske, G., Solomon, S. C., 2010.
628 Underplating of the Hawaiian Swell: Evidence from teleseismic receiver
629 functions. *Geophysical Journal International* 183 (1), 313–329.
- 630 Minarik, W., Watson, E. B., 1995. Interconnectivity of carbonate melt at low
631 melt fraction. *Earth Planet Sci. Lett.* 133, 423–437.
- 632 Ohtani, E., Litasov, K., Tomofumi, H., Kubo, T., Kondo, T., jun 2004. Water
633 transport into the deep mantle and formation of a hydrous transition zone.
634 *Physics of The Earth and Planetary Interiors* 143-144, 255–269.
- 635 Plank, T., Manning, C. E., 2019. Subducting carbon. *Nature* 574 (7778),
636 343–352.
637 URL <http://dx.doi.org/10.1038/s41586-019-1643-z>
- 638 Rychert, C. A., Laske, G., Harmon, N., Shearer, P. M., 2013. Seismic imaging
639 of melt in a displaced Hawaiian plume. *Nature Geoscience* 6 (8), 657–660.
- 640 Schulze, K., Marquardt, H., Kawazoe, T., Boffa Ballaran, T., McCammon,
641 C., Koch-Müller, M., Kurnosov, A., Marquardt, K., 2018. Seismically in-
642 visible water in Earth’s transition zone? *Earth and Planetary Science*
643 *Letters* 498, 9–16.
644 URL <https://doi.org/10.1016/j.epsl.2018.06.021>
- 645 Shearer, P., 1990. Seismic imaging of upper-mantle structure with new evi-
646 dence for a 520-km discontinuity. *Nature* 344, 121–126.
- 647 Sobolev, A. V., Hofmann, A. W., Kuzmin, D. V., Yaxley, G. M., Arndt,
648 N. T., Chung, S.-L., Danyushevsky, L. V., Elliott, T., Frey, F. a., Garcia,

649 M. O., Gurenko, A. a., Kamenetsky, V. S., Kerr, A. C., Krivolutskaya,
650 N. a., Matvienkov, V. V., Nikogosian, I. K., Rocholl, A., Sigurdsson, I. a.,
651 Sushchevskaya, N. M., Teklay, M., apr 2007. The amount of recycled crust
652 in sources of mantle-derived melts. *Science (New York, N.Y.)* 316 (5823),
653 412–7.

654 Sobolev, A. V., Hofmann, A. W., Sobolev, S. V., Nikogosian, I. K., 2005. An
655 olivine-free mantle source of hawaiian shield basalts. *Nature* 434 (7033),
656 590.

657 Sun, Y., Hier-Majumder, S., Xu, Y., Walter, M., 2020. Stability and migra-
658 tion of slab-derived carbonate-rich melts above the transition zone. *Earth
659 and Planetary Science Letters* 531, 116000.
660 URL <https://doi.org/10.1016/j.epsl.2019.116000>

661 Tauzin, B., Debayle, E., Wittlinger, G., 2010. Seismic evidence for a global
662 low-velocity layer within the Earth’s upper mantle. *Nature* 3, 718–721,
663 doi:10.1038/NGEO969.

664 Tauzin, B., Ricard, Y., 2014. Seismically deduced thermodynamics phase di-
665 agrams for the mantle transition zone. *Earth and Planetary Science Letters*
666 401, 337–346.

667 Thomson, A. R., Walter, M. J., Kohn, S. C., Brooker, R. A., 2016. Slab
668 melting as a barrier to deep carbon subduction. *Nature* 1 (2005), 1689–
669 1699.

670 Turcotte, D., Schubert, G., 2001. *Geodynamics*. John Wiley & Sons.

- 671 Vinnik, L., Farra, V., 2007. Low S velocity atop the 410-km discontinuity
672 and mantle plumes. *Earth and Planetary Science Letters* 262, 398–412,
673 doi:10.1016/j.epsl.2007.07.051.
- 674 Wei, S. S., Shearer, P. M., 2017. A sporadic low-velocity layer atop the 410km
675 discontinuity beneath the Pacific Ocean. *Journal of Geophysical Research:*
676 *Solid Earth* 122 (7), 5144–5159.
- 677 Wimert, J. T., Hier-Majumder, S., 2012. A three-dimensional microgeody-
678 namic model of melt geometry in the earth’s deep interior. *Journal of*
679 *Geophysical Research-Solid Earth* 117 (B04), B04203.
- 680 Wolfe, C. J., Solomon, S. C., Laske, G., Collins, J. a., Detrick, R. S., Orcutt,
681 J. a., Bercovici, D., Hauri, E. H., Dec. 2009. Mantle shear-wave veloc-
682 ity structure beneath the Hawaiian hot spot. *Science (New York, N.Y.)*
683 326 (5958), 1388–90.
- 684 Wolfe, C. J., Solomon, S. C., Laske, G., Collins, J. a., Detrick, R. S., Orcutt,
685 J. a., Bercovici, D., Hauri, E. H., Mar. 2011. Mantle P-wave velocity struc-
686 ture beneath the Hawaiian hotspot. *Earth and Planetary Science Letters*
687 303 (3-4), 267–280.
- 688 Xu, W., Lithgow-Bertolini, C., Stixrude, L., Ritsema, J., 2008. The effect
689 of bulk composition and temperature on mantle seismic structure. *Earth*
690 *Planet Sci. Lett.* 275, 70–79.